AIMS Mathematics, 7(11): 20292–20312.
DOI: 10.3934/math.20221111
Received: 02 August 2022
Revised: 28 August 2022
Accepted: 04 September 2022
Published: 16 September 2022

http://www.aimspress.com/journal/Math

Research article

New application of MOL-PACT for simulating buoyancy convection of a copper-water nanofluid in a square enclosure containing an insulated obstacle

Fahad Alsharari[1,*] and Mohamed M. Mousa[2,3,*]

[1] Department of Mathematics, College of Science and Arts, Jouf University, Gurayat, 77455, Saudi Arabia
[2] Department of Finance, College of Sciences and Human Studies at Hotat Sudair, Majmaah University, Al-Majmaah 11952, Saudi Arabia
[3] Department of Basic Engineering Sciences, Faculty of Engineering at Benha, Benha University, Benha 13512, Egypt

* **Correspondence:** Email: f.alsharari@ju.edu.sa, mm.mousa@mu.edu.sa.

Abstract: In this study, we have simulated transient and steady state free convection flow and heat transfer inside a square enclosure filled with a copper-water nanofluid of spherical shape nanoparticles following Tiwari-Das model. The cavity containing an insulated rectangular obstacle of height ranging from 0% to 50% of the cavity side-length. The vertical sides of the enclosure are kept at different temperatures, while the flat sides are assumed to be adiabatic as the obstacle. The combined method of lines/penalty-artificial compressibility technique (MOL-PACT) has been applied to solve the dimensional time dependent mathematical model after converting it into a non-dimensional structure. The combined method of lines/penalty-artificial compressibility technique is recently successfully applied to simulate free convection of MHD fluid in square enclosure with a localized heating. The extension of this promising technique for studying heat transfer of nanofluids is one of the objectives of this paper. Another objective of the study is to inspect the impact of several model parameters such as, the obstacle height, nanoparticles volume-fraction, nanoparticles radius and Rayleigh number on streamlines, temperature distribution and Nusselt number as an expression of heat transfer inside the enclosure. The results have been discussed and shown graphically. Comparisons with former results for related cases in the literature are made and reasonably good agreements are observed.

Keywords: nanofluid; buoyancy convection; heat transfer; method of lines; artificial compressibility technique
Mathematics Subject Classification: 65M06, 76R10

Abbreviations:

Nomenclature	ρ: density [kg/m^3]
G: gravitational acceleration [m/s^2]	μ: dynamic viscosity [kg/m.s]
Ra: Rayleigh number	α: thermal diffusivity [m^2/s]
Pr: Prandtl number	k: thermal conductivity [W/m.K]
Nu: Nusselt number	β_T : thermal expansion coefficient [1/K]
L: enclosure side-length [m]	φ: nanoparticles volume fraction
h: obstacle height [m]	β: ratio of the nanolayer thickness to the original particle radius
d: obstacle width [m]	
x, y: Cartesian coordinates [m]	ψ: stream function [m^2/s]
t: time [s]	**Subscripts**
p: fluid pressure [N/m^2]	H: hot side
T: temperature [K]	C: cold side
u: velocity component in the x direction [m/s]	avg: averaged
v: velocity component in the y direction [m/s]	NF: nanofluid
n: nanoparticles shape factor	W: Water
b: penalty parameter	Cu: Copper
c: compressibility parameter	**Superscript**
C_p: specific heat [J/kg.K]	*: dimensional variable
χ: mixture ratio	

1. Introduction

The study of heat transfer of buoyancy convection flow in several geometrical cavities has been widely investigated using numerical; analytical; and experimental techniques because of the extensive variety of their requests in engineering and technology such as safety and operation of nuclear reactor, electronic devices cooling systems, solar-thermal collectors, micro-electro-mechanical systems, and so on. Enhancing the heat transfer performance in these systems is an important issue in terms of the proper functionality of these systems and of energy saving as well. As known, the heat transfer of common conventional fluids such as water, oil, and ethylene glycol of low thermal conductivities that can be considered as a fundamental limitation of using such fluids in high-efficiency heat transfer systems because it is very challenging to be content with the representation of such systems [1]. To defeat this problem, an innovative approach to improve the heat transfer, is achieved by applying nanoparticles to the base fluid (nanofluid). The term nanofluid (NF) refers to a mixture of liquid and solid that involves of a base-liquid and nanoparticles of size <100 nano meter. Pure metallic particles such as Cu, Fe, Al and Ag can be used as nanoparticles. Carbon nanotubes and ceramic particles like SiO_2, TiO_2, CuO, and Al_2O_3 are used as nanoparticles as well. The benefit of these nanoparticles lies in that they improve the anomalous growth in effective thermal conductivity (ETC) of the fluid. In [2],

It is noticed that the ETC of the ethylene glycol increases up to 40% by adding copper nanoparticles of approximately mean diameter <10 nano meter to the base ethylene glycol. In [3], Choi et al. concluded that the suspension of nanotubes and oil anomalously enhances effective thermal conductivity of the oil. In [4], Das et al. examined the enhancement in the effective thermal conductivity for the nanofluids with H_2O as a base fluid and CuO or Al_2O_3 particles as suspension nanoparticles rather than using a base fluid only. In [5], Putra et al. performed an experiment investigation to investigate the heat transfer caused by natural convection in a cylindrical enclosure filled with Cu–H_2O, and Al–H_2O nanofluids. They determined that the obvious coalescence of nanoparticles heat transfer, caused by natural convection, is occurred for high Rayleigh number (*Ra*).

Recently, many researchers analyzed heat transfer of nanofluids caused by natural convection inside cavities of several shapes such as rectangular [6–9], trapezoidal [10–13], triangular [14–17] and unusual shapes [18–22]. In most of the investigations have been done, the effects of different parameters on the nanofluids heat transfer in the enclosures are analyzed. In [18], Armaghani et al. investigated the effects of *Ra* and the aspect ratio of a T-shaped cavity on the free convection and entropy of Al_2O_3–H_2O nanofluid. They assumed the flow is laminar and the nanoparticles of spherical shapes. They deduced that the values of cavity aspect ratio and *Ra* have a strong effect on the heat transfer inside the cavity. In [19], Toghraie et al. examined the impact of porous ribs for L-shaped microchannels by considering the properties of the porous media for several Reynolds numbers. The free convection of CuO–H_2O nanofluid inside a corrugated cavity containing a heated obstacle was examined in [20]. The authors applied the Koo-Kleinstreuer Li model to transact with the fluid ETC and viscosity. The effect of parallel fins on a nanofluid of water based carbon nanotubes of single wall was studied by Haq et al. [21]. They determined that the rate of heat transfer increased by expanding the length of the heated fin and reduces by increasing the value of *Ra* and solid volume-fraction of nanoparticles. In [22], Eshaghi et al. investigated the double diffusive natural convection of a hybrid Cu–Al_2O_3–H_2O nanofluid within an H-shaped enclosure having an obstacle at the top side. They studied the impact of Rayleigh and Lewis numbers and buoyancy ratio on the generation of entropy and heat transfer. Other related studies are given in [23–27]. From the literature, one can observe that there are little investigations that consider the impact of an insulated obstacle wall within square cavities.

Recently, the combined method of lines and penalty-artificial compressibility technique (MOL-PACT) is proposed and successfully applied to simulate the MHD convective fluid inside a square enclosure due to localized heating of the bottom side [28]. In this study, we will extend the application of this promising technique to simulate the transient and steady-state heat transfer of a nanofluid subjected to Tiwari-Das model inside a square enclosure having a rectangular insulated obstacle. The optimum values of artificial compressibility and penalty parameters of the numerical technique are estimated using a developed stability restriction. The nanofluid considered in this study is a copper–water mixture with spherical shape nanoparticles. We will examine the impact of thermal and physical parameters like *Ra*, obstacle height, volume-fraction of nanoparticles, ratio between the thickness of nanolayer and the radius of the original solid particles on streamlines, temperature, and heat transfer. The results of this study can be provided useful data that may be used to optimize design and enhance thermal performance of energy systems. The validation of the MOL-PACT results is confirmed by comparing them for special cases with other results presented in the literature.

The structure of the remaining sections are as follows: in the following section, the physical description of the physical and mathematical model is revealed. In Section 3, the numerical procedure

and code validation are given. Section 4 uncovers the investigation results and discussion. The last section is for summarizing of the obtained results and conclusions of this work.

2. Problem description and mathematical model

Consider the motion of an unsteady, laminar, viscous 2D Cu–H_2O nanofluid in a square enclosure of side-length L. We considered that the x-axis is evaluated along the bottom side wall of the enclosure and the y-axis is evaluated along the left side wall. The schematic diagram of the physical and coordinate are displayed in Figure 1. The bottom and top side walls are considered adiabatic and the nanofluid are isothermally cooled and heated by the right and left vertical side walls of the enclosure at constant temperatures of T_C and T_H, respectively where $T_C < T_H$. There is an adiabatic rectangular obstacle that positioned in the middle of the bottom side. The width and height of the obstacle are assigned as d and h, respectively. In this investigation, we consider one case for d and three cases for h as: $d = 0.2\ L$ and $h = 0, 0.25\ L, 0.5\ L$. In the current study, we have chosen water (H_2O) as a base fluid whereas copper (Cu) as nanoparticles. The shapes of the nanoparticles are chosen as spherical ones. The choice of water as a base fluid are considered because of its practical uses in several fields such as cooling of many reactors, solar-thermal collector, etc. This problem and geometry can be happened in many technical applications like solar-collectors, heat-exchangers, and cooling of electronic apparatus and chips that use nanofluids. The adiabatic obstacle may be considered as a model of heat transfer modifier device or controller. In heat exchangers, adiabatic obstacle can be a prototypical of a baffle that manages the process of heat transport and flow rate. In case electronic chips cooling, an adiabatic obstacle may be used for decreasing or increasing the heat transfer from special parts of hot chips.

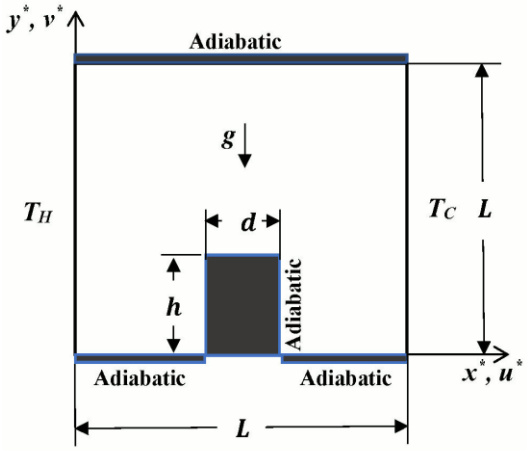

Figure 1. Schematic diagram of the physical model.

It is considered that a thermal balance occurs between the water and copper nanoparticles, and there is no slip between the two components of the nanofluid. Because of the small diameter of nanoparticles, they are simply fluidized. We considered the Cu–H_2O nanofluid as a water including copper nanoparticles as species of water. The physical parameters of the nanofluid are assumed to be

fixed except the change of nanofluid density that appears in the mass force portion of the equation of momentum, that is projected by the Boussinesq-approximation. The acceleration due to gravity acts out in the downward direction of y axis. All the enclosure walls are rigid with no-slip. Essentially, this kind of cavities loaded with such nanofluids is developed as a solar-thermal collector. Based on the aforementioned statements, the fundamental governing equations are presented in a dimensional form as [10,29]:

$$\frac{\partial u^*}{\partial x^*} + \frac{\partial v^*}{\partial y^*} = 0, \tag{1}$$

$$\frac{\partial u^*}{\partial t^*} + u^* \frac{\partial u^*}{\partial x^*} + v^* \frac{\partial u^*}{\partial y^*} = -\frac{1}{\rho_{NF}} \frac{\partial p^*}{\partial x^*} + \frac{\mu_{NF}}{\rho_{NF}} \left(\frac{\partial^2 u^*}{\partial x^{*2}} + \frac{\partial^2 u^*}{\partial y^{*2}} \right), \tag{2}$$

$$\frac{\partial v^*}{\partial t^*} + u^* \frac{\partial v^*}{\partial x^*} + v^* \frac{\partial v^*}{\partial y^*} = -\frac{1}{\rho_{NF}} \frac{\partial p^*}{\partial y^*} + \frac{\mu_{NF}}{\rho_{NF}} \left(\frac{\partial^2 v^*}{\partial x^{*2}} + \frac{\partial^2 v^*}{\partial y^{*2}} \right) + \frac{(\rho \beta_T)_{NF}}{\rho_{NF}} g(T^* - T_C), \tag{3}$$

$$\frac{\partial T^*}{\partial t^*} + u^* \frac{\partial T^*}{\partial x^*} + v^* \frac{\partial T^*}{\partial y^*} = \frac{k_{NF}}{(\rho Cp)_{NF}} \left(\frac{\partial^2 T^*}{\partial x^{*2}} + \frac{\partial^2 T^*}{\partial y^{*2}} \right). \tag{4}$$

The meanings and dimensions of symbols describe nanofluid physical and thermal properties, that appear in equations and forthcoming formulas, are listed in the nomenclature. These properties like nanofluid density, viscosity, thermal diffusivity, heat capacity, thermal conductivity, and coefficient of thermal expansion. The next expressions are employed to compute the physical and thermal properties of Cu–H_2O nanofluid:

The following formula that presented by Brinkman [30] was used as an expression for the nanofluid effective viscosity μ_{NF}:

$$\mu_{NF} = \frac{\mu_W}{(1-\varphi)^{\frac{5}{2}}}, \tag{5}$$

where μ_W is the viscosity of base fluid (water) and φ is the copper nanoparticles volume-fraction. The effective viscosity of many nanofluids in the different temperature ranges are experimentally investigated and measured by many researchers. The results of these investigations demonstrated reasonably great agreement with the Brinkman theory [30]. Respectively, the nanofluid effective-density, thermal-diffusivity, heat-capacitance and the coefficient of thermal-expansion are provided in [10,29,31] as:

$$\rho_{NF} = \varphi\, \rho_{Cu} + (1-\varphi)\rho_W, \tag{6}$$

$$\alpha_{NF} = \frac{k_{NF}}{(\rho Cp)_{NF}}, \tag{7}$$

$$(\rho Cp)_{NF} = \varphi\, (\rho Cp)_{Cu} + (1-\varphi)(\rho Cp)_W, \tag{8}$$

$$(\rho \beta_T)_{NF} = \varphi\, (\rho \beta_T)_{Cu} + (1-\varphi)(\rho \beta_T)_W. \tag{9}$$

Concerning the ETC of nanofluid k_{NF}/k_W, there are many models in nanofluids [32,33]. In [33],

Maxwell informed that nanofluid ETC depends on the base liquid thermal-conductivity and solid particles volume-fraction and shape. He also concluded that the ETC of spherical type nanoparticles raises as the nanoparticles volume-fraction raise. In addition to the influence of the volume-fraction of the solid particles on the nanofluid thermal-conductivity, it is also affected by the shape of nanoparticles for non-spherical particles. One of the famous models of the ETC, of nanofluids with non-spherical particles, that proposed by Hamilton and Crosser [34] is given below

$$\frac{k_{NF}}{k_W} = \frac{[k_{Cu}+(n-1)k_W+(n-1)(k_{Cu}-k_W)\varphi]}{[k_{Cu}+(n-1)k_W-(k_{Cu}-k_W)\varphi]}, \tag{10}$$

where n is the nanoparticles shape-factor of. The shape factor takes values ranging from 0.5 to 6.0. For example, $n = 3$ for spherical shape particles while $n = 4.9$ for cylindrical shape particles [35]. Because of nanofluids may comprise of solid nanoparticles, a bulk liquid and solid-like nanolayers, Yu and Choi [36] suggested an alternative formula for determining the ETC of nanofluids of spherical shapes solid particles as:

$$\frac{k_{NF}}{k_W} = \frac{[k_{Cu}+2k_W+2(1+\beta)^3(k_{Cu}-k_W)\varphi]}{[k_{Cu}+2k_W-(1+\beta)^3(k_{Cu}-k_W)\varphi]}, \tag{11}$$

where the embedding parameter β is the fraction between the nanolayer thickness and the original solid particles radius. This model gives a reasonably good results when contrasted with experimental results in the literature for nanoparticles having diameters <10 nano meter [36]. We used this model to characterize the ETC of the considered nanofluid in this study.

The appropriate initial/boundary conditions for the model are specified below:

• For $t^* < 0$;

- $u^* = v^* = p^* = T^* = 0$,

• For $t^* \geq 0$;

- at the top and bottom boundaries of the cavity and obstacle: $u^* = v^* = \partial T^*/\partial y^* = 0$,
- at the left and right boundaries of the obstacle: $u^* = v^* = \partial T^*/\partial x^* = 0$,
- at the left boundaries of the enclosure: $u^* = v^* = 0$, $T^* = T_H$,
- at the right boundaries of the enclosure: $u^* = v^* = 0$, $T^* = T_C$.

To nondimensionalize the considered model equations (1)–(4), the following non-dimensional replacements are applied:

$$\left.\begin{aligned} x = \frac{x^*}{L}, y = \frac{y^*}{L}, t = \frac{\alpha_W t^*}{L^2}\ u = \frac{u^* L}{\alpha_W}, v = \frac{v^* L}{\alpha_W}, p = \frac{p^* L^2}{\rho_W \alpha_W^2}, \\ T = \frac{T^*-T_C}{T_H-T_C},\quad Pr = \frac{\mu_W}{\rho_W\, \alpha_W},\quad Ra = \frac{g(\beta_T)_W\, \rho_W L^3 (T_H-T_C)}{\mu_W\, \alpha_W} \end{aligned}\right\} \tag{12}$$

Substituting Eqs (5) and (12) into Eqs (1)–(4), yields the following dimensionless shape of the model equations

$$\frac{\partial u}{\partial x} + \frac{\partial v}{\partial y} = 0, \tag{13}$$

$$\frac{\partial u}{\partial t} + u\frac{\partial u}{\partial X} + v\frac{\partial u}{\partial y} = -\frac{\rho_{\mathbb{W}}}{\rho_{NF}}\frac{\partial p}{\partial X} + Pr\left(1-\varphi\right)^{-5/2}\left(\frac{\rho_{\mathbb{W}}}{\rho_{NF}}\right)\left(\frac{\partial^2 u}{\partial x^2} + \frac{\partial^2 u}{\partial y^2}\right), \tag{14}$$

$$\frac{\partial V}{\partial t}+u\frac{\partial V}{\partial X}+v\frac{\partial V}{\partial y}=-\frac{\rho_{W}}{\rho_{NF}}\frac{\partial p}{\partial y}+Pr\left(1-\varphi\right)^{-5/2}\left(\frac{\rho_{W}}{\rho_{NF}}\right)\left(\frac{\partial^2 V}{\partial X^2}+\frac{\partial^2 V}{\partial y^2}\right)+PrRa\frac{\left(\beta_T\right)_{NF}}{\left(\beta_T\right)_{W}}T, \tag{15}$$

$$\frac{\partial T}{\partial \tau}+u\frac{\partial T}{\partial x}+v\frac{\partial T}{\partial y}=\frac{\alpha_{NF}}{\alpha_{W}}\left(\frac{\partial^2 T}{\partial x^2}+\frac{\partial^2 T}{\partial y^2}\right), \tag{16}$$

and subjected to the next initial/boundary conditions:

• For $t < 0$;

- $u = v = p = T = 0$,

• For $t \geq 0$;

- at the top and bottom boundaries of the cavity and obstacle: $u = v = \partial T/\partial y = 0$,
- at the left and right boundaries of the obstacle: $u = v = \partial T/\partial x = 0$,
- at the left boundaries of the enclosure: $u = v = 0$, $T = 1$,
- at the right boundaries of the enclosure: $u = v = 0$, $T = 0$.

The motion of the nanofluid can be well described by the stream-function ψ that gained from the velocity components as below [11,28]:

$$u=\frac{\partial \psi}{\partial y}, v=-\frac{\partial \psi}{\partial x}. \tag{17}$$

The relations in Eq (11) directs to the well-known Poisson's equation, for finding the stream-function ψ [11,28],

$$\frac{\partial^2 \psi}{\partial x^2}+\frac{\partial^2 \psi}{\partial y^2}=\frac{\partial u}{\partial y}-\frac{\partial v}{\partial x}. \tag{18}$$

Because of the non-slip conditions at all the boundaries of the enclosure and obstacle, we set $\psi = 0$ at all these boundaries when solving the Poisson's equation (18). The results of ψ are obtained by solving the discretized version of Eq (18) using successive over relaxation (SOR) method with an appropriate accuracy after obtaining the results of the velocity components u and v.

The variation of heat transfer of the nanofluid along the hot left side wall can be physically described using the local-Nusselt number (Nu) and averaged-Nusselt number (Nu_{avg}) that are given below:

$$Nu=-\frac{\partial T}{\partial x}\Big|_{x=0}, \tag{19}$$

$$Nu_{\text{avg}}=\int_0^1 Nu\, dy. \tag{20}$$

The thermophysical properties of H_2O as a base fluid and Cu as nanoparticles are given in Table 1.

Table 1. Thermophysical properties of H_2O and Cu.

Property	Water (H_2O)	Copper (Cu)
ρ [kg/m^3]	997.1	8933
C_p [J/kg.K]	4179	385
$\beta_T \times 10^{-5}$ [1/K]	21	1.76
k [W/m.K]	0.613	400
$\alpha \times 10^{-7}$ [m^2/s]	1.47	1163.1
Pr	6.2	-

3. Numerical procedure, stability, and validation

3.1. Penalty-artificial compressibility technique

Corresponding to the penalty-artificial compressibility technique (PACT) [28], we introduce the next penalty-artificial compressibility equation (PACE) instead of the continuity one (13),

$$\frac{\partial p}{\partial t} = -c^2\left(\frac{\partial u}{\partial x} + \frac{\partial v}{\partial y}\right) - b\,\frac{\partial}{\partial t}\left(\frac{\partial u}{\partial x} + \frac{\partial v}{\partial y}\right), \tag{21}$$

where the artificial compressibility parameter c and the penalty parameter b can be estimated form a stability restriction that obtained by applying the linearized Fourier stability analysis to the method of lines (MOL) finite difference scheme.

3.2. Method of lines and stability analysis

In order to apply the MOL, the space coordinates x and y of the physical domain and the governing equations (14)–(16) and the PACE (21) are discretized with $M\times M$ uniformly 2D mesh points where $x_k = x_{k\text{-}1} + \delta x$, $y_l = y_{l\text{-}1} + \delta y$, $x_0 = x_0 = 0$, $x_M = x_M = 1$, $k, l = 1, 2, \ldots, M$ and $\delta x = \delta y = 1/M$, where δx and δy are step size in x and y directions, respectively. Making a discretization using 2nd order central finite difference approximation to the derivatives of the dependent variables (u, v, p, T) with respect to spatial variables x and y in Eqs (14)–(16) and (21), as proposed in [28], yields a system of ordinary differential equations (ODEs) that can be easily solved using any time integrator technique. Here we used the 4th order Runge–Kutta method that built in Maple software with a time step δt as a time integrator.

Following the same approach used in [28] to estimate the parameters b and c, produces the next stability restriction:

$$\delta t[(\delta x)^{-2} + (\delta y)^{-2}]\left[c^2\delta t + 2b + 2Pr(1-\varphi)^{-\frac{5}{2}}\frac{\rho_W}{\rho_{NF}}\right] < 1. \tag{22}$$

The strategy for estimating the parameters b and c is based on disregarding the convection terms the forward Euler explicit representation of Eqs (14)–(16) and (21); and applying the linearized von Neumann stability analysis [37].

Setting $\delta^2 = ((\delta x)^{-2} + (\delta y)^{-2})^{-1}$ and presenting a mixture ratio χ as,

$$\chi = \frac{c^2\delta t}{2\left[b + Pr(1-\varphi)^{-5/2}\frac{\rho_W}{\rho_{NF}}\right]}, \tag{23}$$

yield the new formulation of the stability condition (22) as

$$\frac{2\delta t}{\delta^2}\left[b + Pr(1-\varphi)^{-\frac{5}{2}}\frac{\rho_W}{\rho_{NF}}\right](\chi+1) < 1. \tag{24}$$

Here, we propose a safety factor s, where $0 < s < 1$, to calculate a value of b form the inequality (24) as,

$$b = \frac{s\,\delta^2}{2\delta t(\chi+1)} - \left[Pr(1-\varphi)^{-\frac{5}{2}}\frac{\rho_W}{\rho_{NF}}\right]. \tag{25}$$

Therefore, the value of c^2 can be easily calculated from Eq (23) as,

$$c^2 = \frac{s\,\delta^2\chi}{(\delta t)^2(\chi+1)}. \tag{26}$$

For given values of mesh parameters, χ, s, Pr, φ, ρ_W, ρ_{NF} and a suitable small value of δt, we can calculate the of values of b and c^2 needed for the stability of the numerical scheme.

All results in the last section are calculated for $s = 0.8$ and $\chi = 1$, mesh size of 40 × 40 points and time step $\delta t = 10^{-5}$. The optimum value of the ratio χ is chosen up on calculating and analyzing the relative error at the continuity equation (13) for various values of χ varying from 10^{-4} to 10^4. These evaluations aren't shown in this study to avoid lengthening in the paper. The chosen mesh size is taken up on a forthcoming grid independence study.

The steady state solution is obtained if the next condition is satisfied for all dependent variables.

$$\sum_{k,l}\left|\Theta_{k,l}^{m+1} - \Theta_{k,l}^{m}\right| < 10^{-5}, \tag{27}$$

where Θ refers to dependent variables u, v, T, p or ψ, while k, l and m represent step indices of x, y and t respectively. From the obtained results, we noticed that the condition (27) is satisfied for all considered cases at $t = 0.5$. Hence, we considered that the solution at this time represents the problem steady-state solution.

3.3. Grid independence study

For purpose of grid independency, the results have been obtained for three uniform meshes: G1: 20 × 20, G2: 40 × 40 and G3: 50 × 50. The variable for which we test the grid independency is the steady state averaged Nusselt number Nu_{avg} for $Ra = 10^6$, $h = 0$, $\beta = 0.1$, $\varphi = 0$ and $\varphi = 0.2$. The results of grid independence study for the considered three meshes are shown in Table 2.

Table 2. Grid independency for $Ra = 10^6$, $h = 0$, $\beta = 0.1$, $\varphi = 0$ and $\varphi = 0.2$.

Mesh	$M \times M$	$\varphi = 0$		$\varphi = 0.2$	
		Nu_{avg}	%Change	Nu_{avg}	%Change
G1	20×20	9.225	-	12.841	-
G2	40×40	9.208	0.18	12.796	0.35
G3	50×50	9.211	0.03	12.798	0.02

Table 2 illustrates that the variation of Nu_{avg} between the mesh G1 and the mesh G2 is 0.18% for $\varphi = 0$ and 0.35% for $\varphi = 0.2$, while the variation between the mesh G2 and the mesh G3 is about 0.03% for $\varphi = 0$ and 0.02% for $\varphi = 0.2$. Therefore, the mesh G2 was used as the mesh size along this investigation.

3.4. Numerical code validation

To validate the developed numerical technique and code, we obtained results for a non-nanofluid (non-NF) case ($\varphi = 0$) when the enclosure had no obstacle ($h = 0$) and filled with air ($Pr = 0.7$) and then compared these results with the benchmark findings in [38] obtained by De Vahl Davis and with

results of Mousa in [8]. This comparison, displayed in Table 3, illustrates that there are excellent agreements between the present results of the MOL-PACT and results obtained in [8,38]. The code of the numerical scheme was also validated by comparing the present results of Nu_{avg} at steady state with the results obtained by Kahveci [39] for several values of β and φ when $h = 0$, $Pr = 6.2$ and $Ra = 10^5$. This comparison, presented in Table 4, shows an excellent agreement between both results. Therefore, the current validations demonstrate the reliability of the numerical results of this work. A full comparison between the current results and corresponding results obtained by Kahveci [39] is displayed in Table 5.

Table 3. A Comparison of steady state Nu_{avg} of the current results with those of [8,38] when $h = 0$, $\varphi = 0$ and $Pr = 0.7$ for many values of Ra.

Ra	Present	De Vahl Davis [38]	Mousa [8]
10^4	2.2444	2.243	2.2447
10^5	4.5181	4.519	4.5209
10^6	8.8054	8.800	8.8187

Table 4. A Comparison of steady state Nu_{avg} of the current results with results of Kahveci [39] when h=0, $Pr = 6.2$ and $Ra = 10^5$ for many values of β and φ.

β	φ	Present	Kahveci [39]
0.02	0.1	5.281	5.384
	0.2	5.756	5.937
0.1	0.1	5.554	5.662
	0.2	6.339	6.537

Table 5. A comparison for the steady state Nu_{avg} between present results and results of Kahveci [39].

Ra		10^4		10^5		10^6	
φ	β	Present	Kahveci [39]	Present	Kahveci [39]	Present	Kahveci [39]
0.1	0.02	2.498	2.553	5.281	5.384	10.458	10.656
	0.1	2.622	2.679	5.554	5.662	11.020	11.227
0.2	0.02	2.680	2.776	5.756	5.937	11.582	11.921
	0.1	2.949	3.052	6.339	6.537	12.796	13.163

4. Results and discussion

In this section, we discuss the obtained results of MOL-PACT for simulating 2D transient and steady-state buoyancy convection flow and heat transfer inside a square cavity having an adiabatic rectangular obstacle and filled with Cu–H_2O nanofluid of spherical shape nanoparticles. The results are illustrated by calculating temperature distribution, streamlines, local and averaged Nusselt number (Nu_{avg}) for different values of the following parameters: $Ra = (10^4, 10^5, 10^6)$, $h = (0, 0.25, 0.5)$, $\beta = (0.02, 0.1)$ and $\varphi = (0.1, 0.2)$. The simulation is done to analyse the impact of various parameters on the characteristics of the flow and heat transfer. The software that was used to execute the code is Maple v.2020. The 1-D figures of Nusselt number variations are plotted using Maple v.2020, while the

2-D figures of streamlines and temperature distributions are plotted using Surfer v.10.

Firstly, we represent the time evolution of solution. In this part we will only show the time evolution of averaged Nusselt number from the transient state to the steady state of the nanofluid for various physical parameters. Then the variations in the streamlines and temperature distribution with respect to various physical parameters will be displayed after reaching the steady-state solution at t ≈ 0.5. Figures 2–5 illustrate the variations of the averaged-Nusselt number versus time for various values of the obstacle height, Rayleigh number, volume-fraction of copper nanoparticles and ratio of the nanolayer thickness to the original nanoparticle radius. These figures clearly show the progress of averaged-Nusselt number from the transient state to the steady state along the time. It is shown that, Nu_{avg} is very significant close to t=0 because of the rapid growth in the temperature at the hot left side. Then Nu_{avg} reduces as time propagates and move towards its steady state value at $t \approx 0.5$.

From Figures 2 and 3, We can be notice that the heat transfer inside the encloser improves as the value of Ra increases for non-NF case and nanofluid case as well. The impact of the increase of obstacle height on the heat transfer is inverse the impact of Ra value i.e., as the obstacle height increases, the heat transfer inside the encloser decreases. The impact of the volume-fraction of copper nanoparticles on the Nu_{avg} and heat transfer is displayed in Figure 4. Here, we noticed two cases. The first one is when the obstacle height less than half of the enclosure side length i.e., $h = 0$, $h = 0.25$, while the second case is when the obstacle height greater than or equal half of the enclosure side length i.e., $h = 0.5$.

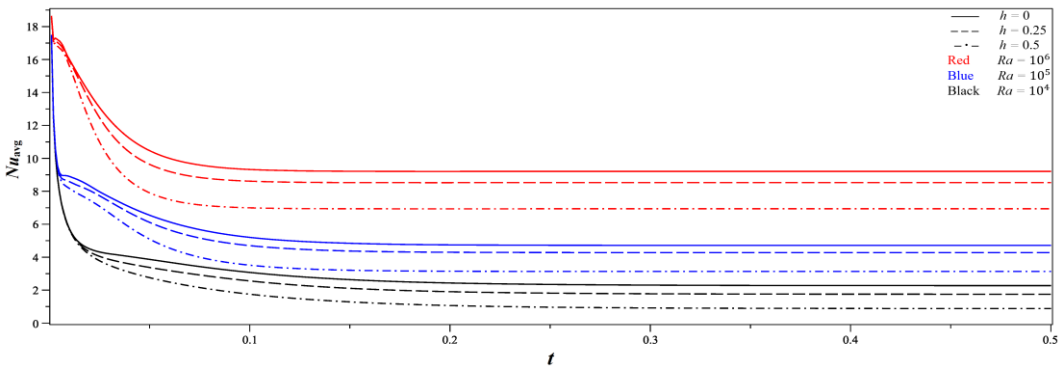

Figure 2. Variations of Nu_{avg} versus t for many values of h and Ra at φ=0 (non-NF).

For the first case, the overall heat transfer improves as the copper nanoparticles volume-fraction increases while when the obstacle height greater than or equal half of the enclosure side length, the overall heat transfer decreases as the copper nanoparticles volume-fraction increases. Figure 5 illustrates the impact of the fraction between the nanolayer thickness and the original solid particles radius on and heat transfer. From this figure, we can say that the increase in the ratio of the nanolayer-thickness to the original nanoparticle radius followed by an increase in the overall heat transfer.

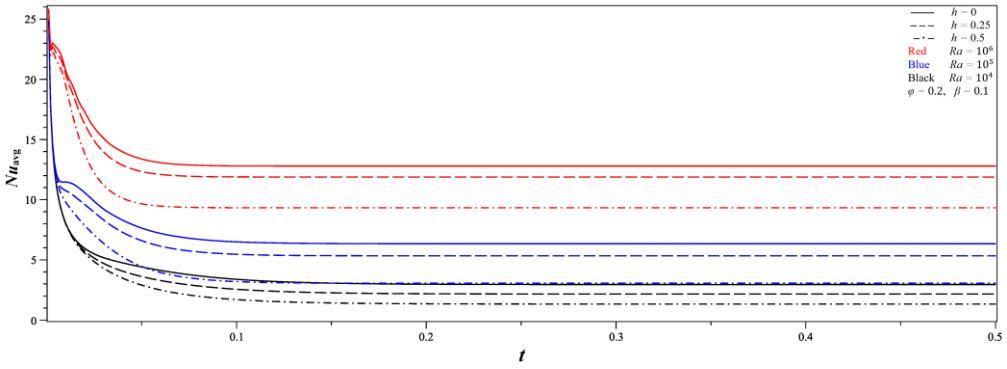

Figure 3. Variations of Nu_{avg} versus t for many values of h and Ra at $\varphi = 0.2$ and $\beta = 0.1$.

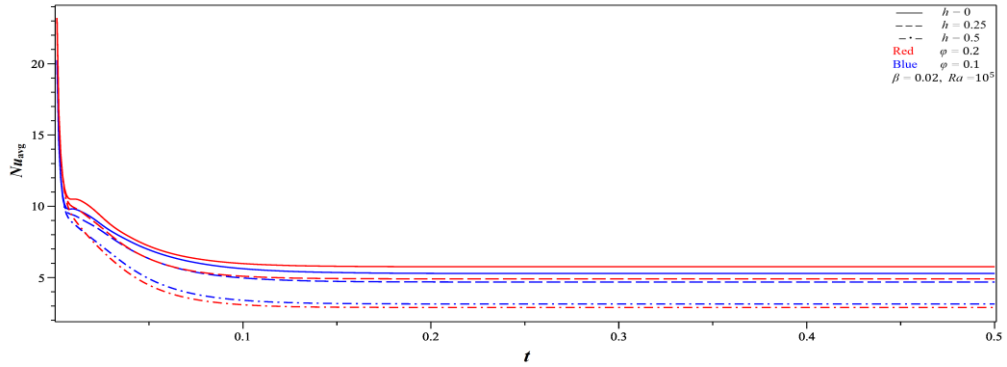

Figure 4. Variations of Nu_{avg} versus t for many values of h and φ at $\beta = 0.02$ and $Ra = 10^5$.

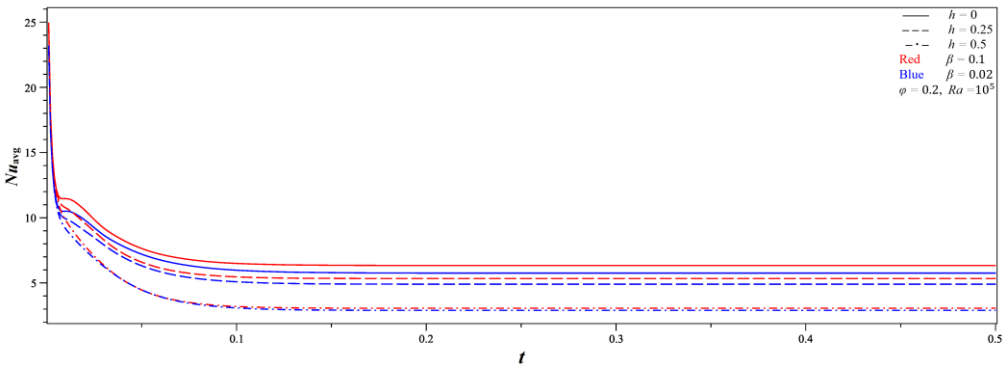

Figure 5. Variations of Nu_{avg} versus t for many values of h and β at $\varphi = 0.2$ and $Ra = 10^5$.

Now, the behavior of the streamlines and temperature distribution will be presented and discussed for several values of the obstacle height, Ra, volume-fraction of nanoparticles and fraction between the nanolayer thickness and the original solid particles radius, but after reaching the steady state solution. Figures 6–9 illustrate the steady state streamlines and temperature distribution in the enclosure at different values of the physical parameters h, Ra, φ and β.

In Figures 6–9, the arrowed contour plots represent the behavior and direction of the flow streamlines while the coloured surface represents the distribution of nanofluid temperature T. The coloured scale displays the temperature intensity inside the cavity. As displayed in these figures, the hot fluid climbs adjacent to the left side wall due to buoyancy forces till it gets the top side wall. Then it moves to right, toward the left cold side wall. Finally, the limit enforced by the bottom side wall pushes the fluid to change direction to left, collecting heat, when it gets the left side wall again. The fluid flow path is achieved as the cold fluid is dragged to the ascent flow along the hot side wall. This circulation, caused by buoyancy forces, is greatly affected by the height of the rectangular obstacle h.

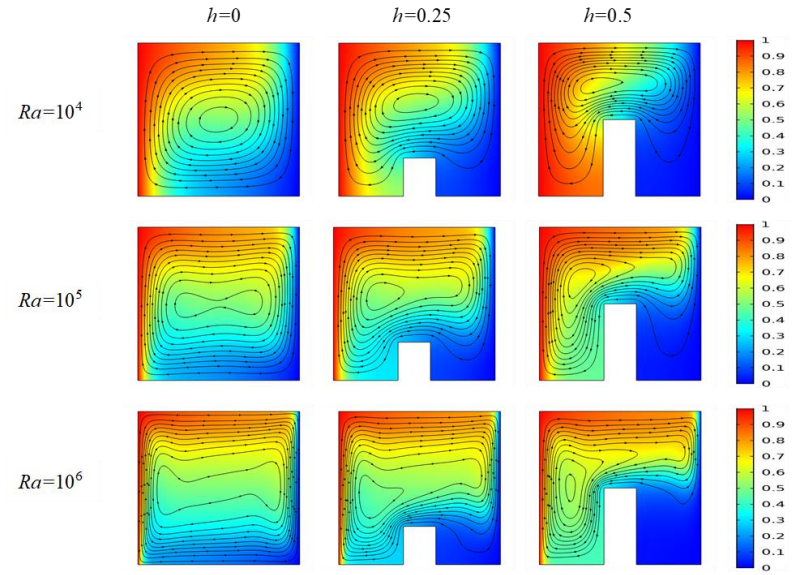

Figure 6. Streamlines and temperature distribution for many values of h and Ra at $\varphi = 0$ (non-NF).

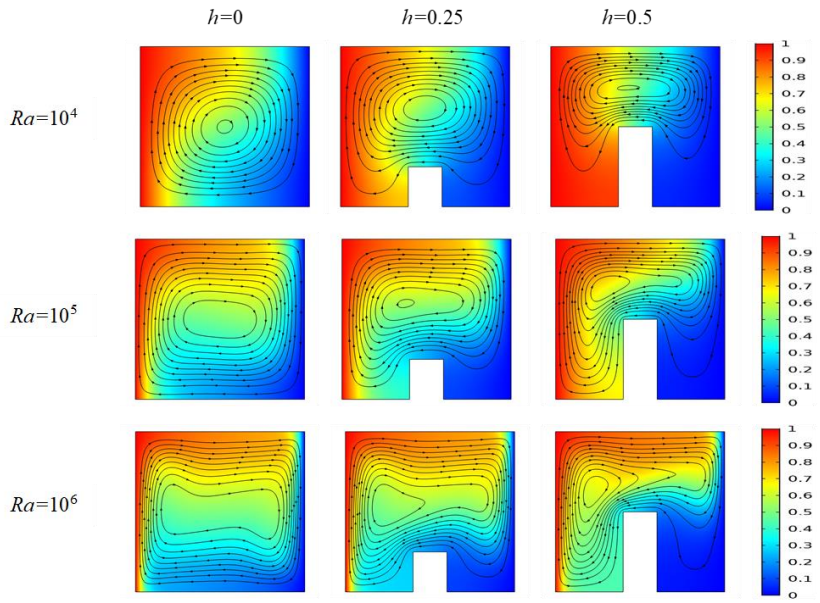

Figure 7. Streamlines and temperature distribution for many values of h and Ra at $\varphi = 0.2$ and $\beta = 0.1$.

As h increases, the buoyancy forces increase and hence the speed of the flow circulation rises resulting in a strong flow circulation and a weak heat transfer. Also, the greater value of Rayleigh number implies more fluid circulation, and more heat will be added to the fluid to increase the nanofluid convection. Moreover, it can be noticed that as Ra increases, the thermal boundary layers become adjacent to each other causing an increase in temperature-gradients and heat transfer. As the nanoparticles volume-fraction φ increases, thermal-diffusion enhances and hence the isotherms become regularly parallel to the hot side wall. Also, the heat transfer in the cavity enhances as the value of φ increases. The effect of the fraction between the nanolayer thickness and the original solid particles radius on the flow and temperature distribution can be shown Figure 9.

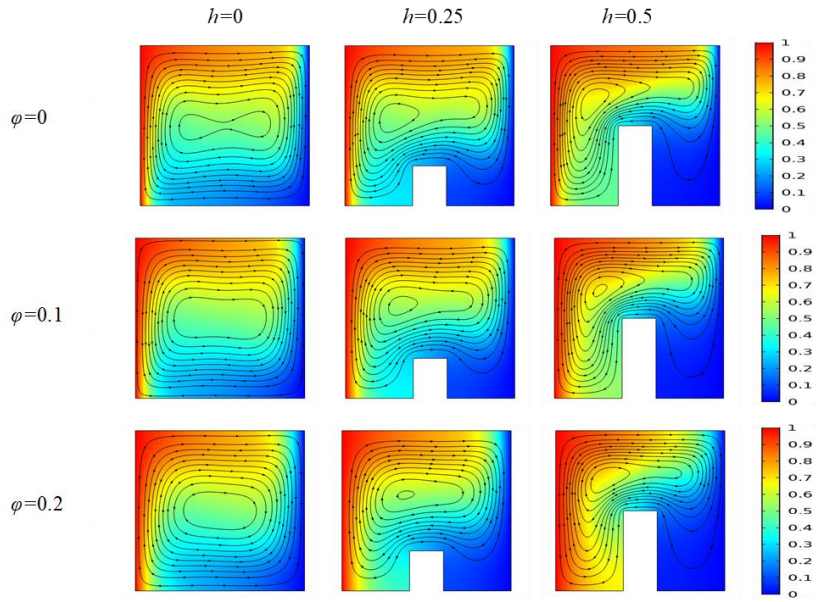

Figure 8. Streamlines and temperature distribution for many values of h and φ at $\beta = 0.1$ and $Ra = 10^5$.

It is known that the radius of the nanoparticles hasn't a significant impact on the solid-like nanolayer. Therefore, the lower values of β relate to the higher values of nanoparticles radius. From Figure 9, it can be noticed that the intensity of fluid movement takes on lower values as the nanoparticles radius increases. It is worth to mention that the effect of β on temperature distribution is very small and isn't noticed in Figure 9.

To examine the impact of the obstacle height, Rayleigh number, nanoparticles volume-fraction and fraction between the nanolayer thickness and the original solid particles radius on the rate of heat transfer inside the cavity, it is essential to visualize the local-Nusselt number along the left hot side wall.

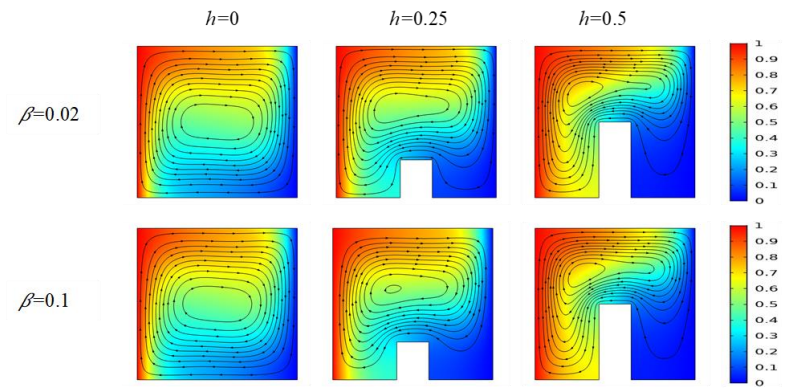

Figure 9. Streamlines and temperature distribution for many values of h and β at φ=0.2 and Ra=10^5.

Figures 10–13 show the variations of steady state Nu at several values of physical parameters h, Ra, φ and β. As displayed in Figures 10 and 11, the strength of the fluid circulation increases because of increasing the buoyancy forces due to the increase of the value of Ra. This causes a growth in the local-Nusselt number Nu along the hot side wall. Because of a strong circulation causing by high thermal energy transport from the hot side to the nanofluid near its surface, therefore the local-Nusselt number takes on high values with the increase of solid-volume fraction. In fact, high rates of thermal-conductivity are supplemented by high rates of thermal-diffusivity. As the value of thermal-diffusivity increases, the temperature-gradient decreases and accordingly the thermal boundary-layer thickness increases. Because the influence of the temperature-gradient due to the existence of nanoparticles is much less significant than the thermal-conductivity ratio, an increasing in the Nusselt number is noticed with the increase in the nanoparticles solid-volume fraction. The impact of increasing obstacle height on the local-Nusselt number is inverse the impact of Rayleigh number values i.e., the local-Nusselt number inside the encloser decreases as the obstacle height increases, while it increases with the increase of Rayleigh number.

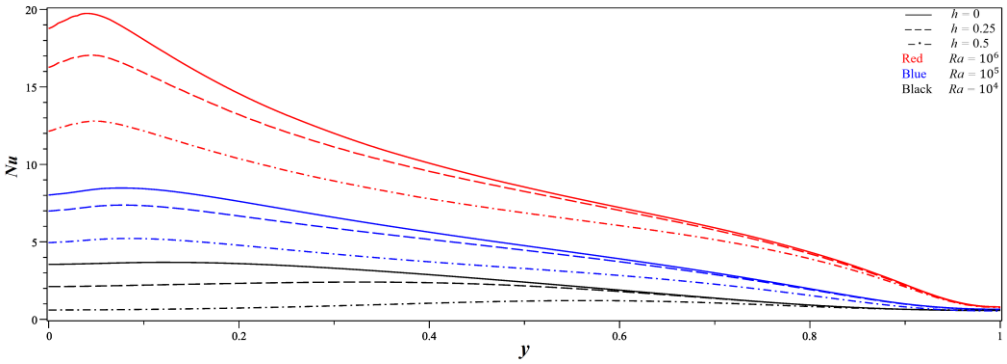

Figure 10. Variations of Nu versus y for many values of h and Ra at φ = 0 (non-NF).

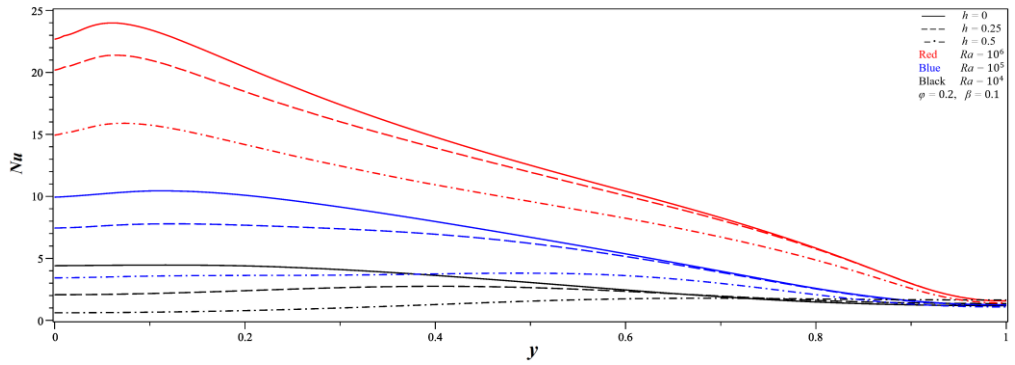

Figure 11. Variations of Nu versus y for many values of h and Ra at $\varphi = 0.2$ and $\beta = 0.1$.

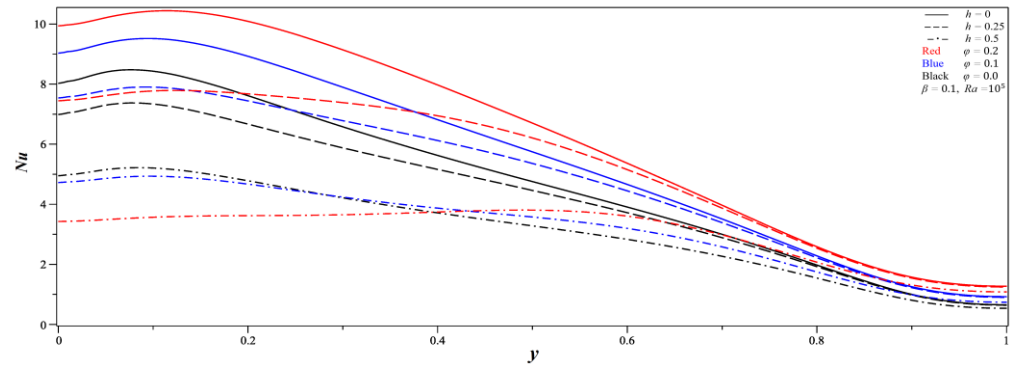

Figure 12. Variations of Nu versus y for many values of h and φ at $\beta = 0.1$ and $Ra = 10^5$.

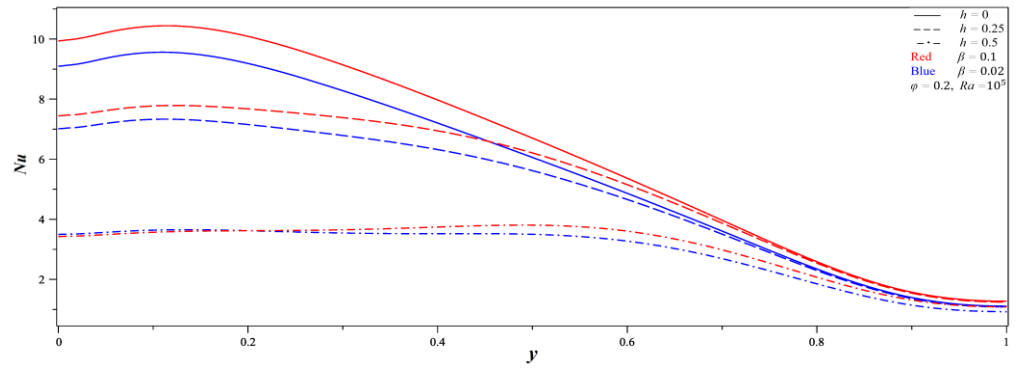

Figure 13. Variations of Nu versus y for many values of h and β at $\varphi = 0.2$ and $Ra = 10^5$.

The effect of the nanoparticles volume-fraction φ on the local-Nusselt number is shown in Figure 12. Generally, because of the impact of the temperature gradient caused by the existence of the nanoparticles is less significant than the effect of thermal conductivity, an increase in the Nu value will be noticed as the value of φ increased. Here, we have two cases. The first case is when the obstacle height less than half of the enclosure side length i.e., $h = 0$, $h = 0.25$, while the second case is when the

obstacle height greater than or equal half of the enclosure side length i.e., $h = 0.5$. For $h = 0$, $h = 0.25$, the local-Nusselt number increases as the volume-fraction of nanoparticles increases along all the left side wall. But for $h = 0.5$, the local-Nusselt number decreases as the nanoparticles volume-fraction increases at the lower portion of the left side wall until $y \approx 0.41$ and then it rises again by the increase of nanoparticles volume-fraction after $y \approx 0.41$. This explains that the overall heat transfer inside the cavity is highly dependent on the obstacle height. Figure 13 illustrates the effect of radius of nanoparticles on the local Nusselt number. From this figure, we can notice that the value of *Nu* enhances with reducing the radius of nanoparticles. This improvement in the local-heat transfer can be mainly ascribed to the increasing of the effective nanolayer volume-fraction. It can be observed that the local-Nusselt number shows a notable enhancement with reducing radius of nanoparticle. This enhancement in local heat transfer can be ascribed mainly to the increase of nanolayer volume-fraction. The similar dependency of the local and averaged heat transfer rates on the *Ra* , volume-fraction and radius of nanoparticles was also noted in [39–41].

The amount of the heat transfer for all the considered cases is summarized in Table 6, which displays the values of the averaged-Nusselt number in the steady-state for all values of the considered parameters. The values of the averaged heat transfer rates were ordered from the lowest to the highest. As can be noticed from the values presented in Table 6, Nu_{avg} doesn't vary considerably with the increasing the value of φ for low values of *Ra*, due to weak convection. While, for higher values of the *Ra*, there is a notable augmentation in Nu_{avg} with rising the value of φ. Also, for higher values of the *Ra*, there is a remarkable augmentation in Nu_{avg} with reducing the radius of nanoparticles. While the effect of nanoparticles radius on the averaged heat transfer is insignificant for low values of *Ra*. The impact of the obstacle height on the averaged heat transfer rate may be demonstrated by comparing the values of Nu_{avg} in Table 6 for various values of *h*. The averaged-Nusselt number exposes a decreasing trend with the increasing of obstacle height. The minimum value of the averaged heat transfer rate is about 0.88 and occurs for the non-NF case with $h = 0.5$ and $Ra = 10^4$. While the maximum rate of the averaged heat transfer is about 12.796 and occurs for the nanofluid case with $h = 0$, $\beta = 0.1$, $\varphi = 0.2$ and $Ra = 10^6$.

Table 6. Steady state averaged-Nusselt number (Nu_{avg}) for many values of *h*, *Ra*, φ and β.

Ra		10^4			10^5			10^6		
φ	β / *h*	0	0.25	0.5	0	0.25	0.5	0	0.25	0.5
0	-	2.273	1.752	0.880	4.718	4.279	3.136	9.208	8.525	6.938
0.1	0.02	2.498	1.834	0.966	5.281	4.683	3.144	10.458	9.719	7.820
	0.1	2.622	1.918	1.022	5.554	4.907	3.251	11.020	10.246	8.228
0.2	0.02	2.680	1.950	1.166	5.756	4.905	2.898	11.582	10.765	8.501
	0.1	2.949	2.160	1.330	6.339	5.341	3.060	12.796	11.888	9.334

Some cases considered in this work was previously examined by Kahveci [39]. Table 5 shows a comparison between the values of Nu_{avg} obtained by Kahveci [39] for Cu–H_2O nanofluid and the present results of steady state Nu_{avg} for $h = 0$. The comparison reveals that there is a reasonably excellent agreement between the present results and results in [39] for the same corresponding cases. Differences between the current results and the results of Kahveci [39] can be attributed to the difference in the accuracy of the numerical technique used and also to the difference in the accuracy of the integration method used in calculating the averaged-Nusselt number.

5. Conclusions

In this study, we propose a new application of the MOL-PACT to simulate transient and steady state buoyancy convective flow in a square cavity filled by Cu–H_2O nanofluid and contains a rectangular adiabatic obstacle. Expressions of the artificial compressibility and penalty parameters that are convenient with the derived stability condition are obtained. The consideration of several Rayleigh number, nanoparticles' radius, and volume-fraction with three different heights of the obstacle makes the current study more convincing from engineering and applied physics point of views. The time-evolution of heat transfer rate from transient state to steady one was examined in detail for several governing parameters.

It can be summarized that those nanoparticles make a considerably enhancement in the heat transfer rate inside the enclosure. It can be also summarized that the manner of variation in the overall rate of heat transfer is almost linear dependent on with the nanoparticles volume-fraction. The obtained results illustrate that the rate of heat transfer decreases with a rising of the height of the rectangular obstacle. It is worth to mention that the impact of the nanoparticles volume-fraction on the heat transfer rate is related to the obstacle height. There is a remarkable increasing in rate of heat transfer with reducing the radius of nanoparticles for relatively high values of Rayleigh number, while this effect becomes insignificant for low values of the Rayleigh number. The Minimum rate of heat transfer occurs when $\varphi = 0$, $h = 0.5$ and $Ra = 10^4$, while the maximum rate occurs when $\varphi = 0.2$, $\beta = 0.1$, $h = 0$, and $Ra = 10^6$. The reasonably good agreement between the current results and the related ones found in the literature, demonstrate accuracy and reliability of this work.

The novelty of the current investigation lies in the fact that the obtained results are new and may be helpful for the experimentalists to inspect the efficiency of the buoyancy convection inside square cavities having adiabatic obstacles and filled with a nanofluid for a purpose of increasing the overall heat transfer rate. Moreover, the proposed numerical technique could offer CFD scientists avenues of research into its development to simulate such models. It's worth to give MOL-PACT more interest to handle hybrid nanofluids with various thermal conditions around the cavity boundaries.

Acknowledgments

The authors would like to thank the Deanship of Scientific Research at Majmaah University for supporting this work under Project Number (R-2022-280). They also would like to thank Jouf University for their encouragements.

Conflict of interest

The authors declare that there is no conflict of interests.

References

1. G. Lorenzini, C. Biserni, L. A. O. Rocha, Geometric optimization of X-shaped cavities and pathways according to Bejan's theory: Comparative analysis, *Int. J. Heat Mass. Tran.*, **73** (2014), 1–8. https://doi.org/10.1016/j.jare.2021.08.003

2. J. A. Eastman, S. U. S. Choi, S. Li, W. Yu, L. J. Thompson, Anomalously increased effective thermal conductivities of ethylene glycol-based nanofluids containing copper nanoparticles, *Appl. Phys. Lett.*, **78** (2001), 718. https://doi.org/10.1063/1.1341218
3. S. U. S. Choi, Z. G. Zhang, W. Yu, F. E. Lockwood, E. A. Grulke, Anomalous thermal conductivity enhancement in nanotube suspensions, *Appl. Phys. Lett.*, **79** (2001), 2252. https://doi.org/10.1063/1.1408272
4. S. K. Das, N. Putra, P. Thiesen, W. Roetzel, Temperature dependence of thermal conductivity enhancement for nanofluids, *J. Heat Transfer*, **125** (2003), 567–574. https://doi.org/10.1115/1.1571080
5. N. Putra, W. Roetzel, S. K. Das, Natural convection of nano-fluids, *Heat Mass Transfer*, **39** (2003), 775–784. https://doi.org/10.1007/s00231-002-0382-z
6. O. A. Olayemi, K. Al-Farhany, A. M. Obalalu, T. F. Ajide, K. R. Adebayo, Magnetoconvection around an elliptic cylinder placed in a lid-driven square enclosure subjected to internal heat generation or absorption, *Heat Transf.*, **51** (2022), 4950–4976. https://doi.org/10.1002/htj.22530
7. M. K. Moraveji, M. Hejazian, Natural convection in a rectangular enclosure containing an oval-shaped heat source and filled with Fe_3O_4/water nanofluid, *Int. Commun. Heat Mass Tran.*, **44** (2013), 135–146. https://doi.org/10.1016/j.icheatmasstransfer.2013.03.011
8. M. M. Mousa, Modeling of laminar buoyancy convection in a square cavity containing an obstacle, *Bull. Malays. Math. Sci. Soc.*, **39** (2016), 483–498. https://doi.org/10.1007/s40840-015-0188-z
9. B. P. Geridonmez, RBF simulation of natural convection in a nanofluid-filled cavity, *AIMS Mathematics*, **1** (2016), 195–207. https://doi.org/10.3934/Math.2016.3.195
10. S. M. Al-Weheibi, M. M. Rahman, M. S. Alam, K. Vajravelu, Numerical simulation of natural convection heat transfer in a trapezoidal enclosure filled with nanoparticles, *Int. J. Mech. Sci.*, **131–132** (2017), 599–612. https://doi.org/10.1016/j.ijmecsci.2017.08.005
11. M. Mousa, Effects of porosity and heat generation on free convection in a porous trapezoidal cavity, *Therm. Sci.*, **23** (2019), 1801–1811.
12. Z. H. Khan, W. A. Khan, R. U. Haq, M. Usman, M. Hamidf, Effects of volume fraction on water-based carbon nanotubes flow in a right-angle trapezoidal cavity: FEM based analysis, *Int. Commun. Heat Mass Tran.*, **116** (2020), 104640. https://doi.org/10.1016/j.icheatmasstransfer.2020.104640
13. Z. H. Khan, O. D. Makinde, M. Hamid, R. Ul Haq, W. A. Khan, Hydromagnetic flow of ferrofluid in an enclosed partially heated trapezoidal cavity filled with a porous medium, *J. Magn. Magn. Mater.*, **499** (2020), 166241. https://doi.org/10.1016/j.jmmm.2019.166241
14. S. M. Aminossadati, Hydromagnetic natural cooling of a triangular heat source in a triangular cavity with water–CuO nanofluid, *Int. Commun. Heat Mass Tran.*, **43** (2013), 22–29. https://doi.org/10.1016/j.icheatmasstransfer.2013.02.009
15. M. M. Mousa, MHD free convection in a porous non-uniformly heated triangle cavity equipped with a circular obstacle subjected to various thermal configurations, *Mod. Phys. Lett. B*, **34** (2020), 2050354. https://doi.org/10.1142/S0217984920503546
16. F. A. Soomro, R. Ul Haq, E. A. Algehyne, I. Tlili, Thermal performance due to magnetohydrodynamics mixed convection flow in a triangular cavity with circular obstacle, *J Energy Storage*, **31** (2020), 101702. https://doi.org/10.1016/j.est.2020.101702
17. R. Ul Haq, S. S. Shah, E. A. Algehyne, Thermal drift and force convection analysis of nanofluid due to partially heated triangular fins in a porous circular enclosure, *Phys. Scripta*, **96** (2021), 065701.

18. T. Armaghani, A. Kasaeipoor, M. Izadi, I. Pop, MHD natural convection and entropy analysis of a nanofluid inside T-shaped baffled enclosure, *Int. J. Numer. Method. H.*, **28** (2018), 2916–2941. https://doi.org/10.1108/HFF-02-2018-0041
19. D. Toghraie, M. Mahmoudi, O. A. Akbari, F. Pourfattah, M. Heydari, The effect of using water/CuO nanofluid and L-shaped porous ribs on the performance evaluation criterion of microchannels, *J. Therm. Anal. Calorim.*, **135** (2019), 145–159. https://doi.org/10.1007/s10973-018-7254-3
20. R. Ul Haq, M. Usman, E. A. Algehyne, Natural convection of CuO–water nanofluid filled in a partially heated corrugated cavity: KKL model approach, *Commun. Theor. Phys.*, **72** (2020), 085003.
21. R. Ul Haq, S. S. Shah, E. A. Algehyne, I. Tlili, Heat transfer analysis of water based SWCNTs through parallel fins enclosed by square cavity, *Int. Commun. Heat Mass Tran.*, 119 (2020), 104797. https://doi.org/10.1016/j.icheatmasstransfer.2020.104797
22. S. Eshaghi, F. Izadpanah, A. S. Dogonchi, A. J. Chamkha, M. B. B. Hamida, H. Alhumade, The optimum double diffusive natural convection heat transfer in H-Shaped cavity with a baffle inside and a corrugated wall, *Case Stud. Therm Eng.*, **28** (2021), 101541. https://doi.org/10.1016/j.csite.2021.101541
23. A. M. Obalalu, Heat and mass transfer in an unsteady squeezed Casson fluid flow with novel thermophysical properties: Analytical and numerical solution, *Heat Transf.*, **50** (2021), 7988–8011. https://doi.org/10.1002/htj.22263
24. N. Biswas, M. K. Mondal, D. K. Mandal, N. K. Manna, R. S. R. Gorla, A. J. Chamkha, A narrative loom of hybrid nanofluid-filled wavy walled tilted porous enclosure imposing a partially active magnetic field, *Int. J. Mech. Sci*., **217** (2022), 107028. https://doi.org/10.1016/j.ijmecsci.2021.107028
25. N. V. Ganesh, Q. M. Al-Mdallal, G. Hirankumar, R. Kalaivanan, Impact of a hot constructal tree-shaped fin on the convection flow of single wall carbon nanotube water nanofluid inside a sinusoidal enclosure, *Int. Commun. Heat Mass Tran.*, **137** (2022), 106279. https://doi.org/10.1016/j.icheatmasstransfer.2022.106279
26. N. V. Ganesh, Q. M. Al-Mdallal, H. F. Öztop, R. Kalaivanan, Analysis of natural convection for a Casson-based multiwall carbon nanotube nanofluid in a partially heated wavy enclosure with a circular obstacle in the presence of thermal radiation, *J. Adv. Res.*, **39** (2022), 167–185. https://doi.org/10.1016/j.jare.2021.10.006
27. M. S. Alqarni, Thermo-bioconvection flow of Walter's B nanofluid over a Riga plate involving swimming motile microorganisms, *AIMS Mathematics*, **7** (2022), 16231–16248. https://doi.org/10.3934/math.2022886
28. M. M. Mousa, M. R. Ali, W. X. Ma, A combined method for simulating MHD convection in square cavities through localized heating by method of line and penalty-artificial compressibility, *J. Taibah Univ. Sci.*, **15** (2021), 208–217. https://doi.org/10.1080/16583655.2021.1951503
29. R. K. Tiwari, M. K. Das, Heat transfer augmentation in a two-sided lid-driven differentially heated square cavity utilizing nanofluids, *Int. J. Heat Mass Tran.*, **50** (2007), 2002–2018. https://doi.org/10.1016/j.ijheatmasstransfer.2006.09.034
30. H. C. Brinkman, The viscosity of concentrated suspensions and solutions, *J. Chem. Phys.*, **20** (1952), 571. https://doi.org/10.1063/1.1700493

31. D. A. Nield, A. Bejan, *Convection in porous media*, New York: Springer, 2013. https://doi.org/10.1007/978-1-4614-5541-7
32. M. J. Uddin, K. S. Al Kalbani, M. M. Rahman, M. S. Alam, N. Al-Salti, I. Eltayeb, Fundamentals of nanofluids : Evolution, applications and new theory, *Int. J. Biomath. Syst. Biol.*, **2** (2016), 1–32.
33. J. C. Maxwell, On stresses in rarefied gases arising from inequalities of temperature, *Proc. R. Soc. London*, **27** (1878), 304–308. http://doi.org/10.1098/rspl.1878.0052
34. R. L. Hamilton, O. K. Crosser, Thermal conductivity of heterogeneous two-component systems, *Ind. Eng. Chem. Fundamem.*, **1** (1962), 187–191. https://doi.org/10.1021/i160003a005
35. E. V. Timofeeva, J. L. Routbort, D. Singh, Particle shape effects on thermophysical properties of alumina nanofluids, *J. Appl. Phys.*, **106** (2009), 014304. https://doi.org/10.1063/1.3155999
36. W. Yu, S. U. S. Choi, The role of interfacial layers in the enhanced thermal conductivity of nanofluids: A renovated Maxwell model, *J. Nanoparticle Res.*, **5** (2003), 167–171. https://doi.org/10.1023/A:1024438603801
37. E. Isaacson, H. B. Keller, *Analysis of numerical methods*, Dover Publications, 2012.
38. G. De Vahl Davis, Natural convection of air in a square cavity: A bench mark numerical solution, *Int. J. Numer. Meth. Fl.*, **3** (1983), 249–264. https://doi.org/10.1002/fld.1650030305
39. K. Kahveci, Buoyancy driven heat transfer of nanofluids in a tilted enclosure, *J. Heat Transfer*, **132** (2010), 062501. https://doi.org/10.1115/1.4000744
40. S. Mirmasoumi, A. Behzadmehr, Effect of nanoparticles mean diameter on mixed convection heat transfer of a nanofluid in a horizontal tube, *Int. J. Heat Fluid Fl.*, **29** (2008), 557–566. https://doi.org/10.1016/j.ijheatfluidflow.2007.11.007
41. S. Z. Heris, S. G. Etemad, M. N. Esfahany, Experimental investigation of oxide nanofluids laminar flow convective heat transfer, *Int. Commun. Heat Mass Tran.*, 33 (2006), 529–535. https://doi.org/10.1016/j.icheatmasstransfer.2006.01.005

AIMS Press